

Scalable Superconducting Nanowire Memory Array with Row-Column Addressing

April 1, 2025

Owen Medeiros^{1*}, Matteo Castellani¹, Valentin Karam¹,
Reed Foster¹, Alejandro Simon¹, Francesca Incalza¹,
Brenden Butters¹, Marco Colangelo^{1, 2}, Karl K. Berggren^{1*}

¹Department of Electrical Engineering and Computer Science,
Massachusetts Institute of Technology, 77 Massachusetts Ave.,
Cambridge, 02139, Massachusetts, USA.

²Department of Electrical and Computer Engineering, Northeastern
University, 360 Huntington Ave, Boston, 02115, Massachusetts, USA.

*Corresponding author(s). E-mail(s): omedeiro@mit.edu;
berggren@mit.edu;

Abstract

Developing ultra-low-energy superconducting computing and fault-tolerant quantum computing will require scalable superconducting memory. While conventional superconducting logic-based memory cells have facilitated early demonstrations, their large footprint poses a significant barrier to scaling. Nanowire-based superconducting memory cells offer a compact alternative, but high error rates have hindered their integration into large arrays. In this work, we present a superconducting nanowire memory array designed for scalable row-column operation, achieving a functional density of 2.6 Mb/cm². The array operates at 1.3 K, where we implement and characterize multi-flux quanta state storage and destructive readout. By optimizing write and read pulse sequences, we minimize bit errors while maximizing operational margins in a 4×4 array. Circuit-level simulations further elucidate the memory cell's dynamics, providing insight into performance limits and stability under varying pulse amplitudes. We experimentally demonstrate stable memory operation with a minimum bit error rate of 10⁻⁵. These results suggest a promising path for scaling superconducting nanowire memories to high-density architectures, offering a foundation for energy-efficient memory in superconducting electronics.

Keywords: superconducting nanowire electronics, cryogenic memory array, energy-efficient storage

Main

The advancement of superconducting computing and fault-tolerant quantum systems depends on developing scalable, energy-efficient cryogenic memory architectures [1]. While superconducting logic circuits have progressed significantly, the lack of dense and reliable memory has remained a critical bottleneck. Existing superconducting memories, primarily based on Josephson junctions (JJs), face fundamental challenges in scaling due to their large unit cell footprints [2, 3]. These limitations have motivated the exploration of alternative device architectures and materials that can reduce bit-cell area while maintaining low power operation and non-volatility [4].

Superconducting loops have long been explored for cryogenic memory applications due to their ability to store information in the form of persistent circulating currents, offering zero static power dissipation and nonvolatile storage while in the superconducting state [5–8]. Traditional JJ-based loop memories, including vortex-transition (VT) cells [9], have demonstrated functional densities of 1 Mbit/cm². However, the geometric inductance required to accommodate a single flux quantum, $\Phi_0 = LI$, constrains further scaling, since reducing the loop area demands a higher drive current to induce a phase transition [4]. This trade-off between cell size and power consumption has increased interest in alternative memory designs that bypass these geometric constraints [10].

Scaling superconducting memory to smaller footprints has driven the exploration of alternative loop-based designs beyond conventional Josephson junctions. Abrikosov vortex RAM (AVRAM) achieves the smallest reported memory cell, with a bit area of 1 μm^2 using focused ion beam junctions and vortex traps [4]. However, this approach has not yet been demonstrated in large arrays and may face integration challenges due to its reliance on non-standard fabrication processes.

Superconducting nanowire memory (SNM or nMem) offers a scalable alternative to conventional superconducting memories, using compact loop-based cells that exploit kinetic rather than geometric inductance [11–14]. Because $L_k \gg L_g$, the cell size is not constrained by loop area and, in principle, can scale down to the superconducting coherence length ξ_0 [12]. A prior demonstration of an 8 bit SNM array achieved a functional density exceeding 1 Mbit/cm² [15], validating the viability of planar row–column addressing architectures for nanowire-based memory.

While these early results established feasibility, practical scalability remained limited by high error rates during word-line activation. These errors arose from a disproportionate increase in cell inductance, which reduced the separation between readout signal levels and increased bit errors [15].

To address this challenge, we redesigned the SNM cell to maintain a constant inductive ratio between word-line off and on states, ensuring stable signal margins during readout. This modification reduced the bit error rate from 10^{-3} to 10^{-5} , matching

the performance of standalone cells even in larger arrays. These improvements demonstrate the feasibility of scaling SNM to higher densities and integrating memory into larger cryogenic systems.

In this work, we fabricated and characterized a 16-bit SNM array using a planar row-column architecture with a functional density of 2.6 Mbit/cm². Although our array density only moderately surpasses the state-of-the-art (1 Mbit/cm²) [9], it reflects an unoptimized design. We expect substantially higher densities to be achievable with targeted layout and fabrication optimization. The array operated at a base temperature of 1.3 K and supported destructive read and write operations using short voltage pulses. We optimized pulse parameters to minimize bit error rate while maximizing threshold margins. We achieved a minimum BER of 1×10^{-5} at 1 MHz and demonstrated robust memory retention across hold times from 2 μ s to 20 s. The measured performance confirms the viability of SNM arrays for scalable cryogenic memory applications.

Superconducting Nanowire Memory Array

In this memory architecture, information is stored as a persistent current in a superconducting loop, with the direction of circulation encoding the logical state. Changing the sign of the write pulse reverses the direction of the induced persistent current.

To ensure robust and deterministic switching, we chose the write-pulse amplitude so that the left hTron (H_L) transitions to the normal state while the right hTron (H_R) remains superconducting. We achieved this selective switching by engineering asymmetries in both critical currents and loop inductances: we designed H_L with a lower critical current than H_R and set the loop inductance such that $L_L \ll L_R$. As a result, a larger fraction of the write-current flows through the left branch, causing H_L to switch before H_R . After we remove the pulse, the resulting circulating current becomes trapped in the loop, preserving the logical state.

Although the loop asymmetry enables deterministic switching in an isolated cell, this design does not inherently support scalable array operation. The architecture includes an additional control mechanism to enable multiple cells within a column: an enable current that selectively heats the targeted cell. This local heating lowers the critical current of the superconducting channel, facilitating switching, but also increases its inductance. Compensating for this thermally induced inductance shift is central to ensuring scalable memory operation.

The fundamental switching element is the heater-cryotron (hTron[12, 16–18]), a superconducting electrothermal device. The hTron consists of a superconducting channel that is locally driven normal via Joule heating from an adjacent normal-metal heater. Its switching threshold is governed by the heater (or enable) current, I_{enable} , which modulates the channel’s critical current, as characterized by Karam et al. [19].¹

In addition to the hTron, each memory cell includes a variable kinetic inductor that remains superconducting but exhibits a temperature-dependent kinetic inductance, $L_K(T)$. Structurally, it is identical to the hTron aside from a constriction that locally

¹The hTron can also function as a standalone memory element, with the stored state encoded in the impedance of the superconducting channel[18].

reduces the critical current. When the enable-current is applied, the resulting local heating increases the inductance of the right branch, maintaining the loop asymmetry condition across thermal states: $L_L(T_{\text{sub}}) \ll L_R(T_{\text{sub}})$ at the substrate temperature, and $L_L(T_{\text{enable}}) \ll L_R(T_{\text{enable}})$ when the enable-current is active. Where T_{sub} is the substrate temperature and T_{enable} is the channel temperature during enable operation. This dynamic inductance compensation is critical for reliable operation in an array configuration[20].

The memory array was implemented by tiling the SNM unit cell in a row–column architecture, enabling scalable addressing. Each unit cell consists of two hTrons and a variable kinetic inductor, as shown in Figure 1a. The circuit elements were patterned from a 23 nm-thick niobium nitride (NbN) superconducting thin film deposited on a thermal oxide wafer. A normal-metal enable line, galvanically isolated from the superconducting layer by a 100 nm silicon dioxide layer deposited via plasma-enhanced chemical vapor deposition (PECVD), provides local temperature control during write and read operations. Figure 1b shows a three-dimensional rendering of the memory stack-up, and Figure 1c displays a false-colored scanning electron micrograph of the fabricated 16 bit array.

Thermal crosstalk between adjacent cells is minimal due to the highly localized nature of hTron heating. The array density used here was chosen to ensure negligible thermal interaction between cells; denser packing is possible with additional design considerations.

The array was wirebonded to a printed circuit board (PCB) and thermally anchored to a 1.3K stage in a closed-cycle cryostat (Figure 1d). Room-temperature electronics supplied the input (bit line) and enable (word line) signals to the device.

Figure 1e presents measured voltage traces during a write operation, corresponding to the signal paths (colored arrows) indicated in panel **d**. The write-pulse polarity determines the direction of the stored persistent current, while a subsequent, unipolar read-pulse retrieves the stored logical state. Each trace is a time average over 500 consecutive acquisitions to improve signal-to-noise ratio.

The memory does not have a controlled initial state and may contain trapped flux. However, when the initial state matters, the system can clear flux by driving the loop into the normal state.

The bottom panel of Figure 1e shows typical readout voltages for logical 0 and 1 states. Histograms of the read voltages across $200 \cdot 10^3$ repeated measurements are shown in Figure 1f. We observed nine W1R0 (write 1, read 0) errors and no W0R1 (write 0, read 1) errors. The shape of the read one distribution is broader due to the additional variability introduced by the hot spot.

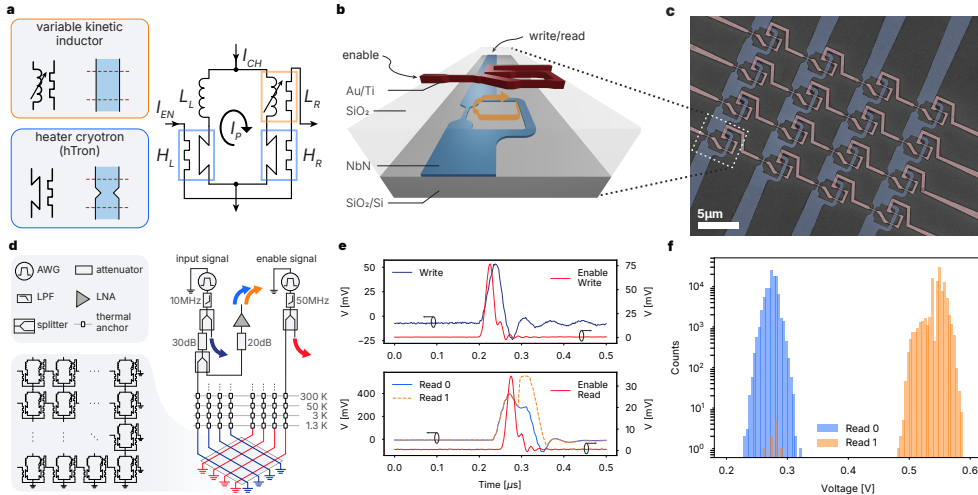


Fig. 1 Superconducting nanowire memory array. **a**, Schematic of a memory unit cell composed of a superconducting loop incorporating two hTrons and a variable kinetic inductor. The cell is biased via two current ports labeled I_{EN} and I_{CH} , corresponding to the enable and channel (write/read) currents, respectively. The superconducting channel is shown in blue, and the heater location is indicated by red dashed lines. An additional constriction in the hTron ensures switching occurs preferentially at the heater site. **b**, Three-dimensional rendering of the memory cell stack. A niobium nitride (NbN) film, patterned on a thermal oxide wafer, forms the superconducting columns. A gold layer defines the normal-metal rows and is galvanically isolated from the NbN by a 100 nm silicon dioxide layer. **c**, False-colored scanning electron micrograph of a 16 bit memory array, highlighting the superconducting columns (blue) and normal-metal rows (red). **d**, Schematic of the experimental setup. Bit-line (input) and word-line (enable) signals are delivered to the array, which is mounted on a PCB and thermalized to 1.3 K inside a closed-cycle cryostat. Abbreviations: AWG, Arbitrary Waveform Generator; LPF, Low Pass Filter; LNA, Low Noise Amplifier. **e**, Measured voltage traces during a write operation. Signals associated with the superconducting column are plotted with respect to the left axes; those associated with the normal-metal row are referenced to the right axes. The write-pulse (blue) encodes logical states via pulse polarity (positive for 1, negative for 0). The enable-pulse (red), applied concurrently, modulates the critical current of the cell. Measured pulse parameters are listed in Table 1. Typical read voltage traces for both logical states are shown in the bottom panel (0 in light blue, 1 in orange). **f**, Histograms of read voltages for both logical states over $200 \cdot 10^3$ measurements. Nine W1R0 (write 1, read 0) errors were observed, with zero WOR1 (write 0, read 1) errors. The broader distribution for read 1 arises from variations in hot spot size, whereas the narrower read zero distribution reflects the absence of a hot spot and depends on the read-current amplitude.

Characterization of Memory Cell Performance

Throughout this work, we characterized memory cells by measuring the bit error rate (BER) across varying read and write bias conditions. To measure the BER, we arbitrarily assigned logical states (0 or 1) to two distinct, stable amplitudes of the read voltage pulse distribution. Subsequent write and read operations were performed, and the measured read voltages were classified according to these assigned states. If a read measurement differed from the expected logical state (e.g., writing a zero resulted in a voltage amplitude assigned as logical 1, or vice versa), it was counted as an error.

The BER was then computed as the ratio of these mismatches (errors) to the total number of measurements.

Due to the arbitrary assignment of logical states, a BER close to 0 indicates error-free operation aligned with the chosen assignment, whereas a BER close to 1 corresponds to error-free operation with inverted logic (the opposite assignment). A BER of 0.5 represents random outcomes, where logical states are indistinguishable.

Figure 1f demonstrates a representative bimodal distribution of read voltage amplitudes corresponding to the logical states. BER is computed as previously defined, and sweeping the read-current amplitude reveals an optimal bias point where the BER is minimized.

The direction of the persistent current—either nominal or inverted—is determined by the relative timing at which each hTron returns (retraps) to the superconducting state during the write operation. Initially, if the write-current amplitude exceeds only the critical current of the left hTron, the left channel becomes resistive first. After the write-pulse ends, the left hTron retraps to the superconducting state while the right hTron remains superconducting throughout, resulting in a nominal persistent current direction.

At higher write currents, both left and right hTron critical currents are exceeded, causing both channels to switch temporarily to a resistive state. In this scenario, as the write-pulse decays, the left hTron cools and returns to superconductivity before the right hTron. This sequence of retrapping causes the persistent current to circulate in the opposite (inverted) direction.²

At the lowest write temperature (marked blue in Fig. 2a,b), the critical current of each hTron was greater than the write current, and therefore no persistent current was stored during the write operation, resulting in a BER of 0.5 for all read current amplitudes. At the highest write temperature (red markers), both hTron critical currents are exceeded, similarly resulting in no persistent current.

The two intermediate write temperatures (light blue and light red in Fig. 2a,b) allowed for the channel to be programmed to either a nominal or inverting state, respectively. The direction and assigned state convention are shown in the inset of Fig. 2a with leaders connected to the data points where the BER approaches zero and one. Both extremes thus mark operational limits, while intermediate temperatures allow deterministic programming. At each read current amplitude point, the BER was calculated from 10^3 read measurements, ensuring sufficient statistical reliability.

Each measurement in the BER sweep consists of a sequence of write and read operations, executed with a typical period of 1 μ s, as illustrated in the larger inset of Fig. 2a. The channel input signal is shown in black, with each operation labeled below. The output signal is shown in light blue for nominal operation, where a write-one (W1) produces a voltage pulse, and in light red for the inverting case, where a write-zero (W0) produces a voltage pulse. The W0 and W1 pulses had equal amplitudes, differing only in sign, while the read-zero (R0) and read-one (R1) pulses were identical.

Additional pulse sequences were tested to verify that memory cell reliability was independent of input sequence variations. These tests included extra read pulses

²This behavior is confirmed by simulation results and explicitly illustrated in Fig. 3, which details the current dynamics and switching sequence underlying both nominal and inverted operation modes

simulating interactions with other cells in the same column and additional enable pulses to emulate row-access scenarios. Sequences involving sustained activation of the enable line were also investigated to detect potential thermal latch-up effects. None of these variations resulted in an increased BER, confirming robustness against sequence-dependent errors. Further investigation into additional sequence patterns, specifically for the addressing of multiple cells (write to a cell, perform operations on the rest of the array, read from the cell), remains important to conclusively rule out sequence-dependent errors.

Figure 2b presents the calculated channel temperature during write operations as a function of the applied enable-current, derived using the thermal model described by Equation 1. Modulating the enable current effectively tunes the memory cell’s temperature, thus controlling the critical currents of the hTrons and enabling the programming of distinct memory states. The resulting temperature range is between 72 and 76% of the critical temperature, T_c , of the NbN film, which is approximately 12.5 K, indicating the critical current of the selected cell is significantly reduced (see Fig. 2b).

Figure 2c displays BER results from read current sweeps conducted at varying read temperatures, set by adjusting the enable current. In contrast to the write-temperature results (Fig. 2a), varying the read temperature shifted the optimal read current region. The optimal read temperature, approximately 7.5 K, provided a favorable balance: sufficiently elevating the critical current difference between the target and neighboring cells (thus minimizing BER), while remaining below the threshold for thermal latch-up, ensuring robust and stable device operation. The vertical dashed line denotes the memory cell’s critical current without the enable current applied, providing a reference point to contextualize the broad operational range of the device.

Finally, Figure 2d presents the calculated channel temperature during the read operation as a function of the enable current. This temperature was calculated using Equation 1.

Figure 3a shows simulated current amplitudes through the left (H_L) and right (H_R) hTrons during the four fundamental memory operations: write-one (i), write-zero (iii), read-one (ii), and read-zero (iv). Dashed lines indicate the hTron critical currents.

In the write-one operation (i), the loop begins with zero current. The applied write bias splits inductively between the two channels, yielding $i_{H_L} > i_{H_R}$. At 120 ns, the left hTron switches when $i_{H_L} > I_{c,H_L}$, while the right hTron remains superconducting. Current redistribution and removal of the write bias establish a clockwise persistent current, $I_P \approx I_{\text{write}}$.

This persistent current remains in the loop at the start of the read-one operation (ii). The applied read bias adds to i_{H_R} , pushing it above threshold ($i_{H_R} > I_{c,H_R}$), while $i_{H_L} < I_{c,H_L}$ due to the opposing persistent current. Current then redistributes, causing the left hTron to switch and generate a voltage pulse (Fig. 3b). This destructive readout resets the cell; it must be rewritten after each read. The presence or absence of a voltage pulse during readout corresponds to logical states ‘1’ and ‘0’, respectively.

To return the cell to the zero state, the write-zero operation (iii) follows the same procedure as (i), but with an inverted write bias. The left hTron switches ($i_{H_L} >$

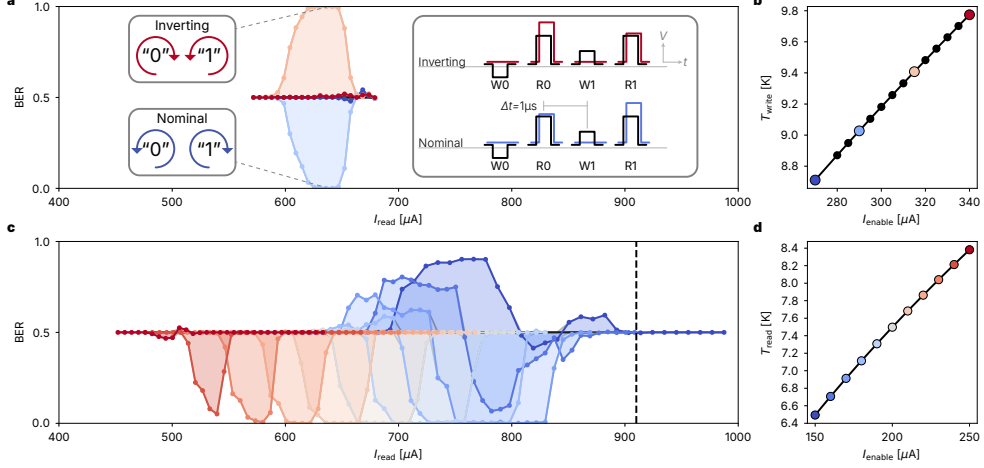


Fig. 2 Readout Fidelity and Operational Modes of a Temperature-Enabled Superconducting Memory Cell. **a**, Measured bit error rate (BER) as a function of read current amplitude at four different write temperatures. A BER approaching 1 corresponds to a deterministic inverting mode, distinct from random errors. The four operational modes are: no switch (blue), nominal (light blue), inverting (light red), and switched (red). Insets with leaders highlight data points where the BER approaches 0 and 1, and indicate the direction of the persistent current for each state. The large inset shows a sketch of voltage versus time describing the write and read inputs used for the BER measurement. Nominal and inverting output traces are sketched in light blue and light red, respectively. **b**, Channel temperature during the write operation as a function of enable current, calculated using equation 1. Colored markers correspond to the read-current sweeps in **a**. **c**, Measured BER as a function of read current amplitude for a sweep of read temperatures. The sweep is performed at temperatures between 6.5 K (blue) and 8.4 K (red), set by the enable-current. The write-current is held constant at 30 μA . The vertical dashed line indicates the critical current of the memory cell without the enable current. **d**, Channel temperature during the read operation as a function of enable current. Colored markers correspond to the read temperature sweeps in **c**.

I_{c,H_L}), while the right hTron remains superconducting, and the resulting persistent current is counter-clockwise, $I_P \approx -I_{\text{write}}$.

Readout in (iv) follows the same sequence as (ii), but with an inverted persistent current present. This reversal modifies the readout conditions: the persistent current now adds to i_{H_L} and subtracts from i_{H_R} , opposite to the read-one case. As indicated by the arrows in panel (iv), i_{H_L} increases but remains below I_{c,H_L} , while i_{H_R} is further suppressed and stays below I_{c,H_R} . Neither hTron switches, and no voltage is produced, as shown in Fig. 3b. The opposite outcomes of panels (ii) and (iv) reflect the sign of the persistent current and enable binary memory operation.

The read current used in panels a and b is indicated by a dashed line in plots c–f.

Although the design targets symmetric heating, the precise temperatures and resulting critical currents of the hTrons are unknown. To account for this and fabrication-related variations, simulations allow independent temperature tuning of the two hTrons.

Figure 3c plots a measured dataset similar to Fig. 2a, but at a fixed write temperature (enable-write current) and varying write-current amplitudes. Sweeping the

write-current amplitude changes the magnitude of the persistent current in the memory cell. At low amplitudes, both hTrons remain superconducting and no current is written to the loop, yielding a BER of $500 \cdot 10^{-3}$ for all read currents. When the write-current amplitude exceeds the left hTron critical current during the write operation, the current is diverted to the right hTron, writing a nominal persistent current. Continued increase of the write current leads to the same behavior until the remaining current after retrapping in the left hTron exceeds the right hTron's critical current, i.e., when $I_{\text{write}} - I_{r,H_L} > I_{c,H_R}$.

In Figure 3c, the transition between nominal and inverted operation occurs at approximately $120 \mu\text{A}$. The inverted persistent current is a result of the left hTron returning to the superconducting state before the right hTron.

Figure 3d plots the measured switching probability as a function of read current amplitude. At low read currents, the memory cell rarely switches; at high currents, switching occurs with near-unity probability.

Figure 3e presents simulated BER for read-current sweeps at three representative write amplitudes: 0, 60, and $300 \mu\text{A}$. The trends capture the same nominal and inverted regimes as in panel c. Quantitative agreement requires further refinement of the simulation model.

Figure 3f shows the simulated switching probability under the same conditions, which mirrors the behavior in panel d. The probability is defined as the ratio of read operations that produce a voltage pulse to the total number of read operations.

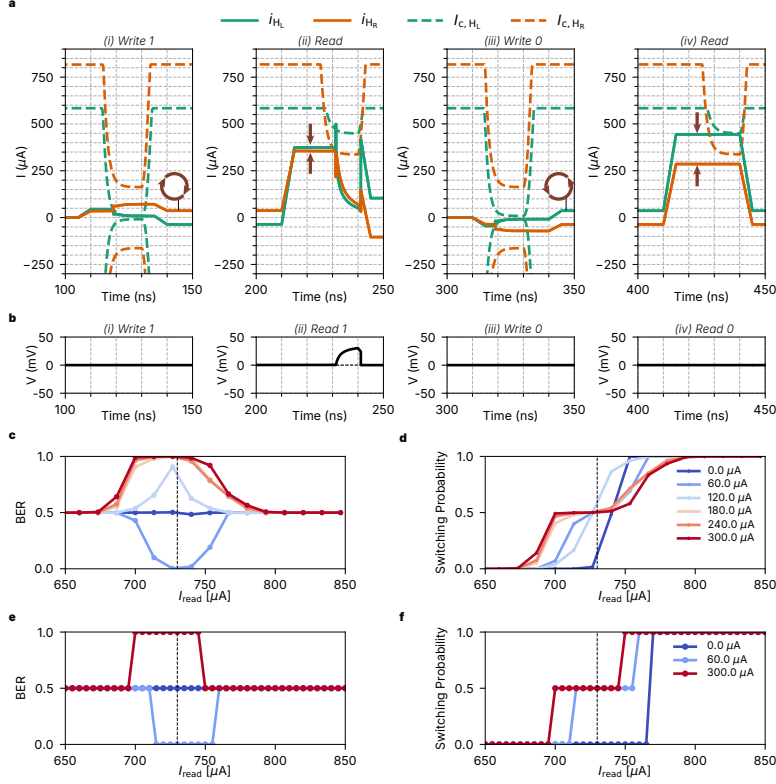


Fig. 3 Simulated and measured operating bounds of the memory cell. **a**, Simulated current amplitudes through the left (H_L , green) and right (H_R , orange) hTrons during memory operations. Dashed lines indicate the corresponding critical currents. Panels i–iv correspond to write-one (W1), write-zero (W0), read-one (R1), and read-zero (R0) operations, respectively. The hTron critical current is plotted as both a positive and negative value for reference to the write-current amplitude. After the write operation, we note the direction of the persistent current with rotating arrows. Before the read operation, arrows show the difference in branch currents due to the persistent current. **b**, Simulated output voltage across the memory cell during each operation in Fig. **a**. No voltage is present during write operations (i, iii), where only H_L transitions to the normal state. A voltage appears during the read-one operation (ii), while the read-zero operation (iv) yields no output, demonstrating nominal readout behavior. **c**, Measured bit error rate (BER) as a function of read current amplitude for various write-current amplitudes. The cell does not operate when $I_W = 0$, shows nominal behavior for $I_W < 120 \mu\text{A}$, and exhibits inverted operation for $I_W > 120 \mu\text{A}$. **d**, Measured switching probability (i.e., voltage detection) during the read operation of cell C3 as a function of read current amplitude. At low read currents, the memory cell rarely switches, while at high currents, switching is nearly deterministic. **e**, Simulated BER for read current sweeps at three representative write-currents: 0, 60, and 300 μA . The trends closely match those observed in panel **c**, with nominal and inverted regimes depending on write amplitude. **f**, Simulated switching probability versus read current amplitude for the same three write-currents as in **e**. The behavior mirrors that in panel **d**, with a sharp transition from low to high switching probability. The black dashed line in **c-f** marks the read-current amplitude used in the simulations shown in panels **a** and **b**.

Array Operating Limits

For a superconducting memory array to function reliably, precise input parameter selection is essential to prevent unintended state changes in neighboring cells. Column inputs must adhere to the constraint that the sum of read and persistent currents remains below the lowest critical current among unselected memory cells, described as $(I_{\text{read}} + I_{\text{P}}) < I_{\text{c}}(T_{\text{sub}})$. Similarly, row inputs are limited by conditions ensuring the critical current of the selected memory cell, reduced by the enable-current, remains greater than the persistent current ($I_{\text{c}}(T_{\text{enable}}) > I_{\text{P}}$), while still being lower than that of unselected cells ($I_{\text{c}}(T_{\text{enable}}) < I_{\text{c}}(T_{\text{sub}})$).

To establish these operating constraints, we extensively characterized the bit-error rate (BER), as summarized in Figure 4. Figure 4a illustrates the measured BER for cell C1 as a function of the enable-write current (I_{enable}), with distinct traces corresponding to write-currents (I_{write}) ranging from 5 μA (blue) to 100 μA (red). Increasing I_{enable} gradually lowers the critical current of the memory cell, initially switching the left hTron and redirecting current into the right hTron branch. If the redirected current surpasses the right hTron critical current, an inverting state is programmed, clearly indicated by peaks in the BER data. Nominal and inverting operational peaks appear centered near enable currents of 280 μA and 305 μA , respectively, broadening with increased write-currents.

Using these measurements, Figure 4b delineates the operating region boundaries extracted from the BER traces. Boundaries were identified based on when the BER deviated within a $\pm 5\%$ range around 0.5, marking transitions between nominal and inverting states. This plot shows that the operating margin depends on the write current for values less than 30 μA , but becomes less dependent on write current for larger values. While approximate, this plot provides a useful guide for selecting write and enable currents to ensure reliable operation of the memory cell.

Figure 4c explores the write-current dynamics at a fixed write temperature by performing linear sweeps of write-currents from 0 μA to 300 μA , across multiple temperatures defined by varying enable currents for cell C3. Additionally, we see that write currents beyond 60 μA lead to an increase in the minimum BER, indicating that a greater fraction of write pulses switch both hTrons to the normal state, leading to a higher probability of inverting the persistent current.

Extracting critical switching currents from these BER traces, as presented in Figure 4d, allowed identification of minimum and maximum operational write-currents. Bounds are just estimates as measurement currents have some uncertainty. This shows that increasing the temperature increases the margin between the minimum and maximum write-currents, but the maximum write-current is limited by the critical current of the right hTron. Once the temperature exceeds the critical temperature, increasing the enable current does not increase the write current margin.

Figure 4e examines memory retention, depicting BER as a function of delay between write and read operations. The same BER measurement sequence was used. The bias conditions were held constant to emphasize the temporal stability of the memory cell, rather than minimize BER at each time point. Error bars correspond to

the standard deviation expected from binomial statistics with $200 \cdot 10^3$ trials. Extending the hold time to 20 s demonstrated robust performance, with zero errors across 100 measurements.

Finally, Figure 4f displays the minimum BER for each memory cell within the 4×4 array, achieved through systematic optimization of read and write voltages. Most cells exhibited BERs below 10^{-3} , except cell C2, which may be affected by suppressed critical currents in a neighboring cell. No systematic spatial variations were detected, underscoring the scalability and uniformity of the superconducting memory array operation.

The calculated power and energy consumption for each memory operation are summarized in Table 1, along with the measured pulse widths (at half maximum amplitude) and relative timing delays between input and enable pulses. Write operations consume minimal energy (46 fJ) compared to enable pulses, which dominate the energy budget (up to 1256 fJ for EW). The read pulse energy is intermediate at approximately 31 fJ. Detailed calculations and methodologies for determining these parameters are provided in the supplementary information, and the pulse definitions correspond to those illustrated in Figure 1.

Table 1 lists the calculated power and energy values for each memory operation. Additionally, we report the width of each pulse (at half max) and the relative delay between input and enable operations. Methods for calculating these values are detailed in the supplementary information.

Table 1 Measured and derived values for: write (W), read (R), enable-write (EW), and enable-read (ER) pulses. Pulse widths and delays were determined at 50% of the peak amplitude. Values are approximate and based on the methodology described in the Methods section, taken from a single device operating at minimum bit error rate.

P_W	1 nW
P_R	368 nW
P_{EW}	57.1 μ W
P_{ER}	9.2 μ W
E_W	46 fJ
E_R	31 fJ
E_{EW}	1256 fJ
E_{ER}	202 fJ
τ_W	40 ns
τ_R	80 ns
τ_{EW}	22 ns
τ_{ER}	22 ns
$\delta\tau_{W,EW}$	2 ns
$\delta\tau_{R,ER}$	15 ns

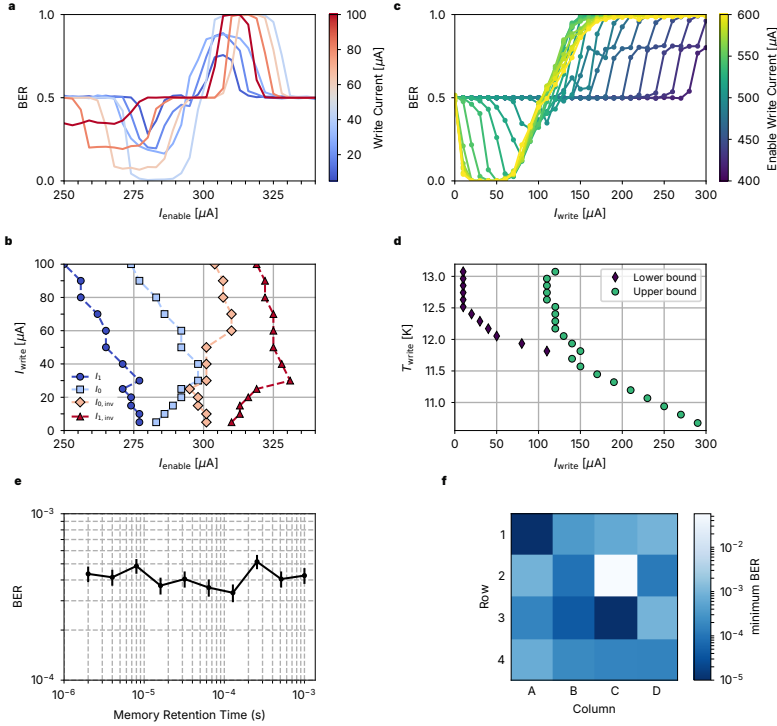


Fig. 4 Operating limits and parameter sensitivity across a memory array. **a**, Measured bit error rate (BER) of cell C1 as a function of enable current, evaluated across several fixed write-current amplitudes. At low write currents, two distinct peaks appear, corresponding to nominal and inverted switching. As the write current increases, the peaks broaden and fidelity improves. Beyond 400 μA , nominal fidelity degrades as the optimal operating region shifts to lower enable currents and becomes narrower. **b**, Enable current bounds extracted from the data in **c**, representing the operational window for each write-current. Bounds are defined as the range over which the BER deviates from 0.5 by more than 5%. **c**, BER of cell C3 as a function of write-current, for a set of enable current amplitudes ranging from 300 to 600 μA in 10 μA steps. Higher enable currents raise the channel temperature during the write operation. **d**, write-current bounds extracted from the data in **c**, using the same $\pm 5\%$ BER deviation criterion. The lower bound corresponds to the minimum write current required to switch the left hTron, while the upper bound marks the regime in which both hTrons exceed their critical currents. **e**, BER as a function of the delay between write and read operations. A single bias point was used for all measurements to emphasize the temporal stability of the memory cell rather than minimize BER at each time point. Each data point represents the average of 2×10^5 trials. **f**, Minimum BER measured for each cell in a 4×4 array, using a 2 μs hold time between write and read operations. Most cells exhibit BERs below 10^{-3} , except C2, which shows elevated error likely due to a reduced critical current in its neighboring memory cell, C3. No systematic spatial variation is observed across the array.

Conclusion

Superconducting computing systems require a scalable, energy-efficient memory architecture—a longstanding gap in the cryogenic electronics stack.

This work demonstrates a 16-bit superconducting nanowire memory array with reliable read–write functionality at 1.3 K, transitioning the technology from individual device demonstrations to array-level integration.

Accessed destructively via nanosecond-scale voltage pulses, the array achieves a minimum bit error rate of $10 \cdot 10^{-6}$ at 1 MHz, with write and read energies of 1.2 pJ and $200 \cdot 10^{-3}$ pJ, respectively. Memory states remain stable for at least 20 s without refresh or error.

The array layout was deliberately kept conservative to simplify fabrication, but the architecture supports aggressive scaling. The memory cell footprint, interconnect pitch, and wiring layer stack can all be reduced in future designs, offering a path toward ultra-dense implementations.

Several technical challenges must be addressed to enable full system integration. The current use of normal-metal enable lines limits power efficiency; although they offer linear thermal control, their resistive nature leads to higher energy dissipation compared to superconducting alternatives. Non-thermal switching approaches, such as gate-controlled superconductivity [21], present a promising route to reduce energy consumption further. Device speed in this study was constrained by the measurement setup, and achieving higher-speed operation will require impedance matching [22] and enhanced signal delivery. Finally, addressing circuitry will need to be integrated either heterogeneously [23, 24] or monolithically [25, 26], depending on fabrication constraints and system architecture.

Although the present system operates at 1.3 K, the architecture is not confined to this regime. Operation up to 4 K appears feasible, and the use of high- T_C materials may allow extension well beyond 4.2 K [27].

The use of niobium nitride (NbN) as the superconducting material was motivated by its high critical temperature and kinetic inductance. Reducing the film thickness could increase the inductance per unit length, enabling even more compact memory designs.

Each memory cell in this demonstration functioned as a single-bit element. Extending the design to support multi-level memory through resistive shunting presents a promising direction for increasing storage density [28].

Overall, this work establishes superconducting nanowire memory as a compact, low-energy, and scalable solution for cryogenic memory. By bridging the gap between high-speed superconducting logic and persistent storage, it lays the groundwork for integration with broader cryogenic systems—including those relevant to artificial intelligence, quantum computing, and photonic networks.

Methods

Thermal Modeling of Memory Cell Operation

A central aspect of this work is the simulation of the memory cell’s thermal response during read and write operations. These operations rely on local Joule heating induced by the enable current, which modifies key physical parameters such as the switching current, retrapping current, thermal conductivity, and the electron and phonon bath temperatures. Rather than extracting these parameters empirically, we simulate the thermal dynamics using a behavioral model of the hTron [19], implemented in LTspice.

By connecting the two hTrons (H_L and H_R) in a loop and performing transient simulations, we capture critical behaviors including switching thresholds, retrapping

characteristics, and persistent current states. This modeling enables the execution of logical operations using realistic current values and operating margins, which is essential for robust array design.

The model depends on fitting parameters that characterize the hTron’s linear thermal response. These parameters are derived by measuring the critical current at various enable currents and extracting the corresponding channel temperature. The temperature of the hTron channel, T_{channel} , is computed from the enable current, I_{enable} , using a phenomenological heating model:

$$T_{\text{channel}} = \left[(T_C^4 - T_{\text{sub}}^4) \left(\frac{I_{\text{enable}}}{I_{\text{enable, max}}} \right)^\eta + T_{\text{sub}}^4 \right]^{1/4} \quad (1)$$

Here, T_C is the film’s superconducting critical temperature, T_{sub} is the substrate temperature, and η is a dimensionless parameter that captures the thermal coupling between the nanowire and the substrate. $I_{\text{enable, max}}$ denotes the maximum enable current applied during calibration.

Using this temperature model, we compute the channel’s critical current as:

$$I_C(T_{\text{channel}}) = I_{C,0} \left[1 - \left(\frac{T_{\text{channel}}}{T_C} \right)^3 \right]^{2.1} \quad (2)$$

With these temperature-dependent parameters, we identify the operating regime of the memory cell, including the amplitude of the stored persistent current and the read/write current margins.

Calculation of Persistent Current and Magnetic Field

The magnitude of the persistent current, determined by the critical current and the inductance of the memory loop, defines the stability (signal-to-noise ratio) and power requirements for memory operations.

The inductance of the memory loop is calculated from the geometric design of the memory cell and the known sheet inductance of the niobium nitride (NbN) film. The loop inductance is given by:

$$L_{\text{loop}} = L_{\text{sheet}} \times \text{area} \quad (3)$$

For a NbN film thickness of 20 nm, the sheet inductance is typically around 20 pH/ \square . The loop area, measured in squares, is computed using finite element analysis and equals the sum of the left (8.7 squares) and right (13.7 squares) branches, totaling 22.4 squares. Thus, the loop inductance is:

$$L_{\text{loop}} = 20 \text{ pH}/\square \times 22.4 \square = 0.448 \text{ nH} \quad (4)$$

The persistent current (I_P) in the memory loop relates to the number of magnetic flux quanta (n) as:

$$I_P = \frac{n\Phi_0}{L_{\text{loop}}} \quad (5)$$

Where Φ_0 is the magnetic flux quantum. Given a persistent current magnitude of $40 \mu\text{A}$ and the calculated loop inductance (0.448 nH), the total magnetic flux stored in the loop is:

$$\Phi = I_P \times L_{\text{loop}} = 40 \mu\text{A} \times 0.448 \text{ nH} = 17.9 \text{ fWb} \approx 10\Phi_0 \quad (6)$$

Due to these small magnitudes of trapped flux, unwanted flux is negligible in device operation and can easily be cleared by applying an enable-current pulse that switches the memory cell, thus ensuring consistent and reliable performance.

Calculation of Power and Energy Dissipation

Power and energy dissipation during memory cell operations are dominated by read and write events, as no energy is consumed in the static storage state. These quantities were calculated using measured currents, voltages, and pulse durations.

During write operations, power dissipation occurs primarily in the left hTron branch and can be approximated by:

$$P_W = I_L V_{\text{hs}} \quad (7)$$

where I_L is the current through the left hTron and V_{hs} is the hotspot voltage. Similarly, power dissipation during read operations is given by:

$$P_R = I_{\text{read}} V_{\text{read}} \quad (8)$$

where V_{read} is the voltage across the read hotspot.

The read hotspot resistance, derived from the normal-state sheet resistance and hotspot area, typically exceeds that of the write hotspot, as both branches can become resistive during readout. Consequently, read operations exhibit higher power dissipation, primarily due to the larger effective hotspot resistance.

Measured read voltage amplitudes yielded a high-state voltage of approximately $540 \cdot 10^{-3} \text{ V}$ and a low-state voltage of $280 \cdot 10^{-3} \text{ V}$, resulting in a difference of $260 \cdot 10^{-3} \text{ V}$. This voltage difference corresponds to a preamplifier output of approximately 0.527 mV , based on a measured gain of 53.87 dB . Using a nominal read current of $736 \mu\text{A}$, the read power (P_R) is calculated as:

$$P_R = 736 \mu\text{A} \times 0.527 \text{ mV} = 388.7 \text{ nW} \quad (9)$$

The corresponding energy dissipated during the read operation is:

$$E_R = P_R \times \tau_R = 388 \text{ nW} \times 80 \text{ ns} = 31.1 \text{ fJ} \quad (10)$$

Direct measurement of the write power is challenging due to the absence of an output voltage pulse and localized dissipation confined to the left branch. However, the write energy is considerably smaller than the read energy and can be estimated from the measured read impedance:

$$Z_{\text{read}} = \frac{V_{\text{read}}}{I_{\text{read}}} = \frac{0.53 \text{ mV}}{736 \text{ } \mu\text{A}} = 0.72 \text{ } \Omega \quad (11)$$

The write power is then approximated by:

$$P_W = I_{\text{write}}^2 Z_{\text{read}} = (40 \text{ } \mu\text{A})^2 \times 0.72 \text{ } \Omega = 1.15 \text{ nW} \quad (12)$$

and the associated energy dissipated during the write operation is:

$$E_W = P_W \times \tau_W = 1.15 \text{ nW} \times 40 \text{ ns} = 46 \text{ fJ} \quad (13)$$

Enable-line power dissipation is computed using the average enable currents and row resistance:

$$P_E = I_E^2 R_{\text{row}} \quad (14)$$

Average measured currents were 185 μA (read) and 460 μA (write), with an average row resistance of 270 Ω . Thus, the enable-line powers for read and write operations were:

$$P_{ER} = (185 \text{ } \mu\text{A})^2 \times 270 \text{ } \Omega = 9.2 \text{ } \mu\text{W} \quad (15)$$

$$P_{EW} = (460 \text{ } \mu\text{A})^2 \times 270 \text{ } \Omega = 57.1 \text{ } \mu\text{W} \quad (16)$$

The corresponding enable energies are:

$$E_{ER} = P_{ER} \times \tau_{ER} = 9.2 \text{ } \mu\text{W} \times 22 \text{ ns} = 202 \text{ fJ} \quad (17)$$

$$E_{EW} = P_{EW} \times \tau_{EW} = 57.1 \text{ } \mu\text{W} \times 40 \text{ ns} = 2284 \text{ fJ} \quad (18)$$

Fabrication Process

While the array yield shown in Figure 4b indicates opportunities for improvement, the fabrication process itself is straightforward and well suited to academic cleanroom environments. It consists of only three lithography steps and uses standard thin-film and etching techniques. Importantly, the hTron operating principle is geometrically scalable [12, 29] and compatible with a broad range of materials and processes [16, 29, 30], making it adaptable to diverse device platforms.

The process begins with a 100 mm thermal oxide wafer, cleaned using a piranha bath. A 23 nm niobium nitride (NbN) film is deposited at 800 °C, resulting in a critical temperature of 12.5 K and a sheet resistance of 78 Ω/\square . From these values, the sheet

inductance is estimated as:

$$L_s \approx \frac{\hbar R_s}{1.76\pi k_B T_C} \approx 8.6 \text{ pH}/\square \quad (19)$$

Pads and alignment markers are formed by liftoff of a 50 nm gold layer with a 5 nm titanium adhesion layer. The memory columns are patterned using ma-N negative resist and etched via reactive ion etching (RIE) in a CF_4 plasma. A 100 nm silicon dioxide dielectric is then deposited using plasma-enhanced chemical vapor deposition (PECVD), patterned photolithographically, and etched by RIE to define via openings. Finally, array rows are defined using ZEP530A resist and completed with a second gold liftoff step.

To improve performance and scalability, future revisions should consider reducing both the NbN and oxide thicknesses and replacing the gold enable line with a superconducting material. The layout may also be optimized for higher density or adapted to foundry-compatible linewidths to support more advanced integration and scaling.

Experimental Setup

To characterize the performance of the memory array, measurements were performed in a cryogenic environment using precision waveform generation, array-specific calibration, and automated optimization routines. This section describes the experimental apparatus, waveform generation strategy, and bit error rate (BER) measurement process.

Cryogenic Measurement Setup. All measurements were conducted under high vacuum ($\sim 10^{-6}$ torr) at a base temperature of 1.3 K. The memory array die, which contained nine separate 16-bit arrays, was bonded to a printed circuit board (PCB) using cryo-compatible epoxy, with aluminum wirebonds connecting the device to PCB traces. Signals were routed from the room-temperature electronics via semi-rigid coaxial cables thermalized at each stage in the cryostat. Two synchronized input signals were generated using an Agilent 33600 arbitrary waveform generator and delivered to the cryostat through microwave splitters (Mini-Circuits ZFRSC-42-S+), low-pass filters (Mini-Circuits SLP-10, SLP-50), and attenuators (VAT-20, VAT-30). The device output signal was combined with the input line, amplified using a MITEQ LNA AM-1309 low-noise amplifier, and digitized by a Teledyne LeCroy WaveRunner760Zi oscilloscope.

Arbitrary Waveform Generation. Waveform amplitudes were calculated from desired current setpoints using an equivalent circuit model. The input channel voltage was derived from a nominal input amplitude of 1 V and the known room-temperature circuit impedance, yielding a reference current I_{nom} . The desired input amplitude was then scaled as:

$$V_{\text{set}} = V_{\text{nom}} \cdot \frac{I_{\text{set}}}{I_{\text{nom}}} \quad (20)$$

A similar procedure was used to determine enable signal amplitudes, based on row-specific resistance values measured at base temperature.

Bit Error Rate Measurement and Optimization. Bit error rate (BER) measurements were performed on each cell in the array using a fixed sequence of write and read pulses (see Fig. 2a). Each cycle included a persistent state duration of $3, \mu\text{s}$, followed by a $1, \mu\text{s}$ delay before initiating the next write. This time was selected to allow for two additional pulses. To evaluate robustness against varying access patterns, we also tested pseudo-random bitstreams and sequences with additional spurious pulses to emulate crosstalk or activation of adjacent cells.

Pulse amplitudes were optimized using Bayesian optimization with Gaussian process regression [31]. After optimization, we verified that the selected parameters generalized across multiple input patterns and operated only when the corresponding cell was enabled.

To characterize retention and timing robustness, BER was measured as a function of delay between write and read operations. For sub-millisecond delays, the timing between pulses was directly modified within the arbitrary waveform sequence. For longer delays ($> 10, \text{ms}$), we employed software-triggered waveforms, incrementally increasing the interval.

Acknowledgments

The authors thank Evan Golden and Phillip D. Keathley for their review during the preparation of this manuscript. This work was funded by the DOE Office of Science Research Program for Microelectronics Codesign through the project ‘Hybrid Cryogenic Detector Architectures for Sensing and Edge Computing Enabled by New Fabrication Processes’ (LAB 212491). Fabrication was carried out in part through the use of MIT.nano’s facilities, with technical guidance from James Daley and Mark Mondol. Initial fabrication development was funded through the Breakthrough Starshot Foundation. O. Medeiros acknowledges support through the National Defense Science and Engineering Graduate (NDSEG) Fellowship Program. A. Simon acknowledges NSF GRFP and MIT Vanu Bose Presidential fellowships. R. Foster acknowledges the Alan McWhorter Fellowship.

References

- [1] Alam, S., Hossain, M. S., Srinivasa, S. R. & Aziz, A. Cryogenic memory technologies. *Nature Electronics* **6**, 185–198 (2023).
- [2] Holmes, D. S. *Cryogenic electronics and quantum information processing*. IEEE (2021).
- [3] Herr, Q., Josephsen, T. & Herr, A. Superconducting pulse conserving logic and josephson-sram. *Applied Physics Letters* **122** (2023).
- [4] Golod, T., Morlet-Decarnin, L. & Krasnov, V. M. Word and bit line operation of a $1 \times 1 \mu\text{m}^2$ superconducting vortex-based memory. *Nature Communications* **14**, 4926 (2023).

- [5] Anacker, W. Potential of superconductive josephson tunneling technology for ultrahigh performance memories and processors. *IEEE Transactions on Magnetics* **5**, 968–975 (1969).
- [6] Zappe, H. A single flux quantum josephson junction memory cell. *Applied Physics Letters* **25**, 424–424 (1974).
- [7] Chen, G., Beasley, M., Horowitz, M., Rosenthal, P. & Whiteley, S. Nondestructive readout architecture for a kinetic inductance memory cell. *IEEE transactions on applied superconductivity* **3**, 2702–2705 (1993).
- [8] Karamuftuoglu, M., Ucpinar, B., Razmkhah, S. & Pedram, M. Superconductor bistable vortex memory for data storage and readout. *Superconductor Science and Technology* **38**, 015020 (2024).
- [9] Semenov, V. K., Polyakov, Y. A. & Tolpygo, S. K. Very large scale integration of josephson-junction-based superconductor random access memories. *IEEE Transactions on Applied Superconductivity* **29**, 1–9 (2019).
- [10] Volk, J., Wynn, A., Golden, E., Sherwood, T. & Tzimpragos, G. Addressable superconductor integrated circuit memory from delay lines. *Scientific Reports* **13**, 16639 (2023).
- [11] Murphy, A., Averin, D. V. & Bezryadin, A. Nanoscale superconducting memory based on the kinetic inductance of asymmetric nanowire loops. *New Journal of Physics* **19**, 063015 (2017).
- [12] Zhao, Q.-Y. *et al.* A compact superconducting nanowire memory element operated by nanowire cryotrons. *Superconductor Science and Technology* **31**, 035009 (2018).
- [13] McCaughan, A. N., Toomey, E., Schneider, M., Berggren, K. K. & Nam, S. W. A kinetic-inductance-based superconducting memory element with shunting and sub-nanosecond write times. *Superconductor Science and Technology* **32**, 015005 (2018).
- [14] Ilin, E. *et al.* Supercurrent-controlled kinetic inductance superconducting memory element. *Applied Physics Letters* **118** (2021).
- [15] Butters, B. A. *et al.* A scalable superconducting nanowire memory cell and preliminary array test. *Superconductor Science and Technology* **34**, 035003 (2021).
- [16] Baghdadi, R. *et al.* Multilayered heater nanocryotron: A superconducting-nanowire-based thermal switch. *Physical Review Applied* **14**, 054011 (2020).

- [17] Alam, S., Rampini, D. S., Oripov, B. G., McCaughan, A. N. & Aziz, A. Cryogenic reconfigurable logic with superconducting heater cryotron: Enhancing area efficiency and enabling camouflaged processors. *Applied Physics Letters* **123** (2023).
- [18] Wang, H. *et al.* Attojoule superconducting thermal logic and memories. *Nano Letters* (2025).
- [19] Karam, V. *et al.* Parameter extraction for a superconducting thermal switch (htron) spice model. *arXiv preprint arXiv:2401.12360* (2024).
- [20] Butters, B. A. *Digital and microwave superconducting electronics and experimental apparatus*. Ph.D. thesis, Massachusetts Institute of Technology (2022).
- [21] Ruf, L., Di Bernardo, A. & Scheer, E. Superconducting non-volatile memory based on charge trapping and gate-controlled superconductivity. *arXiv preprint arXiv:2503.17241* (2025).
- [22] Colangelo, M. *et al.* Impedance-matched differential superconducting nanowire detectors. *Physical Review Applied* **19**, 044093 (2023).
- [23] Zhao, Q.-Y., McCaughan, A. N., Dane, A. E., Berggren, K. K. & Ortlepp, T. A nanocryotron comparator can connect single-flux-quantum circuits to conventional electronics. *Superconductor Science and Technology* **30**, 044002 (2017).
- [24] Fredenburg, J. *et al.* A 32-channel cryo-cmos asic for snspsd biasing and read-out with picosecond timing. Tech. Rep., Fermi National Accelerator Laboratory (FNAL), Batavia, IL (United States) (2024).
- [25] Buzzi, A. *et al.* A nanocryotron memory and logic family. *Applied Physics Letters* **122** (2023).
- [26] Miyajima, S. *et al.* Single-flux-quantum signal processors monolithically integrated with a superconducting nanostrip single-photon detector array. *Applied Physics Letters* **122** (2023).
- [27] Charaev, I. *et al.* Single-photon detection using large-scale high-temperature mgb2 sensors at 20 k. *Nature Communications* **15**, 3973 (2024).
- [28] Onen, M. *et al.* Single-photon single-flux coupled detectors. *Nano Letters* **20**, 664–668 (2019).
- [29] McCaughan, A. N. *et al.* A superconducting thermal switch with ultrahigh impedance for interfacing superconductors to semiconductors. *Nature electronics* **2**, 451–456 (2019).

- [30] Nguyen, M.-H. *et al.* Cryogenic memory architecture integrating spin hall effect based magnetic memory and superconductive cryotron devices. *Scientific reports* **10**, 248 (2020).
- [31] Head, T. Scikit-optimize. <https://github.com/scikit-optimize/scikit-optimize> (2020).